Materials LAB

RESEARCH ARTICLE
Materials Lab 2023, 2, 230014

Enhanced energy storage performance in Gd/Mn co-doped $AgNbO_3$ lead-free antiferroelectric ceramics via tape casting

Qixin Chen[1], Mingyuan Zhao[1,2], Jing Wang[2*] and Lei Zhao[1*]

Antiferroelectric materials are promising for applications in advanced high-power electric and electronic devices. Among them, $AgNbO_3$-based ceramics have gained considerable attention due to their excellent energy storage performance. Herein, multiscale synergistic modulation is proposed to improve the energy storage performance of $AgNbO_3$-based materials, whereby the tape casting process is employed to improve the breakdown strength and Gd/Mn doping is utilized to enhance the antiferroelectric stability. As a result, a high recoverable energy storage density up to 5.3 J cm^{-3} and energy efficiency of 67.6% are obtained in Gd/Mn co-doped $AgNbO_3$ ceramic, which shows good temperature stability and frequency stability. These results show that the components and processes proposed in this work provide a feasible method for improving the energy storage performance of $AgNbO_3$-based ceramics.

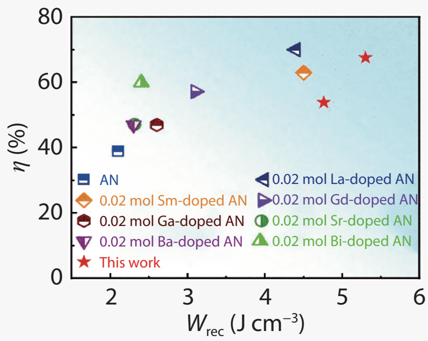

Electronic devices are now evolving toward reducing volume and weight, thus leading to an increasing demand for high-performance energy storage devices.[1,2] Among them, dielectric capacitors have been favored for their excellent power density.[3] Dielectric capacitors have great development prospects in the applications of aerospace medical equipment and power electrical systems.[4,5] Dielectric materials used for capacitors can be divided into four categories: linear dielectrics, ferroelectrics (FEs), relaxor ferroelectrics (RFEs) and antiferroelectrics (AFEs). The recoverable energy storage density W_{rec} and energy efficiency η of dielectric materials can be estimated by the following:

$$W_{st} = \int_0^P E\mathrm{d}P \quad (1)$$

$$W_{rec} = \int_{P_r}^{P_{max}} E\mathrm{d}P \quad (2)$$

$$\eta = \frac{W_{rec}}{W_{st}} \times 100\% \quad (3)$$

where P_r, P_{max} and E represent remnant polarization, maximum polarization, and applied electric field, respectively.[6,7] AFE ceramics have attracted much attention in the field of energy storage because of their double hysteresis loops (*P-E* loops). Among many AFE materials, lead-based AFE materials, such as $(Pb,La)(Zr,Sn)O_3$ and $PbZrO_3$, have commendable energy storage properties.[8] But lead is harmful to the environment and human body, which makes lead-free energy storage materials imperative. $AgNbO_3$ is a lead-free AFE material with typical perovskite structure.[9,10] It undergoes phase transitions of monoclinic (M_1, M_2, and M_3) phase, orthorhombic (O) phase, tetragonal (T) phase and cubic (C) phase with increasing temperature. Among them, M_1 phase is the ferrielectric (FIE) phase, M_2 and M_3 phases are the AFE phase, and the phase transition between them is related to the cation (Ag and Nb) shift. The O, T and C phases are paraelectric phases, and the phase transition between them is related to the inclination of the oxygen octahedron. The phase structure of $AgNbO_3$-based materials can be changed by ions doping.[11,12] $AgNbO_3$ shows many intresting good performances in many fields such as FE photovoltaic, piezoelectric system and photocatalysis.[13–15] The AFE double *P-E* loops of $AgNbO_3$ ceramic were first reported in 2007, which possesses a polarization of 52 μC cm^{-2}. [16] In 2016, Tian *et al.* prepared high-quality $AgNbO_3$ ceramics and obtained a W_{rec} of 2.1 J cm^{-3} at 175 kV cm^{-1}.[17] In 2017, the W_{rec} was increased to 4.2 J cm^{-3} in Ta-doped $AgNbO_3$ ceramics[18], which makes $AgNbO_3$ ceramics a hot topic for energy storage. Enhancing the AFE stability and the breakdown strength (E_b) are important methods to improve the W_{rec} in $AgNbO_3$-based ceramics.[19] The FE/AFE phase stability of the perovskite structures can be judged by the tolerance factor *t*, which is calculated by the following formula:

[1] *Key Laboratory of High-precision Computation and Application of Quantum Field Theory of Hebei Province, College Physics Science and Technology, Hebei University, Baoding 071002, China*
[2] *State Key Laboratory of Mechanics and Control of Mechanical Structures, College of Aerospace Engineering, Nanjing University of Aeronautics and Astronautics, Nanjing 210016, China*
* Corresponding author, E-mail: wang-jing@nuaa.edu.cn; leizhao@hbu.edu.cn

Received 1 March 2023; Accepted 27 April 2023; Published online

© 2023 The Author(s). *Materials Lab* published by Lab Academic Press

DOI: 10.54227/mlab.20230014

$$t = \frac{R_A + R_O}{\sqrt{2}(R_B + R_O)} \quad (4)$$

where, R_A, R_B and R_O are the average radii of A-site cations, B-site cations and oxygen ions, respectively. The ionic radius of corresponding coordination number (CN) should be adopted in calculation, namely CN=6 for B-site cation and CN=12 for A-site cation. t=1 describes an ideal perovskite structure where no distortion of oxygen octahedra occurs. Expect for few compounds with tolerance factor close to unity, most other provskites have varying degrees of distortion at ambient conditions. When t>1, the size of B-site cations is relatively small and the off-center displacement is allowed, giving rise to spontaneous polarization. When t<1, the A-site cation is relatively small and oxygen octahedra tilting occurs to accommodate the coordination environment of the A-site cation. The existence of oxygen octahedra tilting suppresses FE stability and is usually found in most AFEs. In principle, the AFE phase stability can be enhanced by decreasing the tolerance factor.[20] Rare earth elements have the advantage of small ionic radius and high valence state, which can be used to reduce the tolerance factor t and enhance AFE stability by replacing Ag^+ at the A-site.[21,22] Meanwhile, rare earth oxides have high melting points, which inhibit grain growth during sintering, thus enhancing the E_b.[23] Therefore, rare earth ions doping is an effective method to improve the W_{rec} in $AgNbO_3$-based ceramics. For example, Luo *et al*. obtained a W_{rec} of 3.12 J cm^{-3} in 2 mol% La-doped $AgNbO_3$ ceramics.[23] Gao *et al*. achieved a W_{rec} of 4.4 J cm^{-3} in 2 mol% La-doped $AgNbO_3$ ceramics.[24] In 2 mol% Sm-doped $AgNbO_3$ ceramics, the W_{rec} is increased to 4.5 J cm^{-3}.[25] The introduction of 4 mol% Gd in the A-site resulted in a high W_{rec} of 4.5 J cm^{-3}.[26] In addition, Mn doping is able to significantly retain the small P_r and reduce the leakage current, thus improving the energy storage properties of $AgNbO_3$-based ceramics. The W_{rec} of $AgNbO_3$ ceramics was increased to 2.5 J cm^{-3} from 1.6 J cm^{-3} after the addition of 0.1 wt% MnO_2.[27] The preparation process has a great influence on the energy storage performance of ceramics. Recently, tape casting method has attracted extensive attention as a method to improve E_b since it can reduce the porosity and increase the density in ceramics.[6,22,28] The E_b of pure $AgNbO_3$ ceramics prepared by tape casting method is increased to 307 kV cm^{-1}. Because of high E_b, the W_{rec} of pure $AgNbO_3$ ceramics has been increased to 2.8 J cm^{-3}.[28]

In this work, Gd and Mn doped $AgNbO_3$ ceramics are prepared via the tape casting process, in which Gd doping is used to reduce tolerance factor t and optimize the phase structure, Mn doping is used to retain the small P_r and reduce the leakage current, and tape casting process is used to improve the E_b. Taking advantage of the enhanced AFE stability and high E_b, a high W_{rec} of 5.3 J cm^{-3} is achieved in $(Ag_{0.94}Gd_{0.02})NbO_3$-0.3wt%Mn ceramics.

Experimental procedures

$AgNbO_3$, $(Ag_{0.94}Gd_{0.02})NbO_3$ and $(Ag_{0.94}Gd_{0.02})NbO_3$-0.3wt%Mn ceramics (denoted as AN, AG2N and AG2N+Mn, respectively) were prepared with the raw materials of Ag_2O (≥ 99.7%, Shanghai Aladdin Biochemical Technology Co., Ltd.), Nb_2O_5 (≥99.99%, Shanghai Aladdin Biochemical Technology Co., Ltd.), Gd_2O_3 (≥99.99%, Shanghai Aladdin Biochemical Technology Co., Ltd.), and MnO_2 (≥98%, Shanghai Aladdin Biochemical Technology Co. Ltd.). The raw materials were weighted according to stoichiometry and mixed by using a planetary ball mill with anhydrous ethanol under 300 rpm for 24 h. The mixed powders were dried at 80 °C and calcinated at 900 °C for 6 h in oxygen. The calcined powders were milled again, followed by the preparation of the $AgNbO_3$ slurry, which can refer to [28]. The AN, AG2N and AG2N+Mn ceramics are sintered 1080 °C, 1090 °C and 1120 °C for 6 hours in oxygen, respectively.

The crystalline structures of AN, AG2N and AG2N+Mn ceramics were examined using an X-ray diffractometer (XRD; D8 advance, Bruker) with Cu Kα radiation (λ = 1.5405 Å). The Raman spectra were measured by the HR Evolution (Horiba JobinYvon, France). Surface morphology was observed by field emission scanning electron microscope (FEI, Nova NanoSEM 450). The average grain size was calculated from the SEM image using a nano measurer. The dielectric properties were performed (TZDM-RT-800, Harbin Julang Technology Co., Ltd) upon the heating process with the rates of 2 °C min^{-1} at 1 V. The sample thickness was controlled to about 80 μm. Au electrodes about 1 mm in diameter were deposited in the central area. The hysteresis loops (*P-E* loops) were measured in silicone oil with a ferroelectric measurement system at 10 Hz (Precision LC II, Radiant Technologies, Albuquerque, NM, America).

Results and discussion

Fig. 1a shows the surface morphology of AN, AG2N and AG2N+Mn ceramics. All ceramics have good compactness with high relative density over 95 % and clear grain boundaries. The grain size of AN ceramic is 4.99 μm, which decreases to 1.51 μm in AG2N ceramic due to the refractory nature of Gd.[26] Compared with AG2N ceramic, AG2N+Mn ceramic shows larger grain size of 22.63 μm. This is attributed to the increased lattice vacancies generated by the substitutions of Mn ions for Ag^+, Gd^{3+} and Nb^{5+} ions, which increases the mobility of grain boundaries and enhances the material transport, thus making larger grains.[29] In addition, the higher sintering temperature of 1200 °C may also be responsible for the enlarged grain size in AG2N+Mn ceramic. The Weibull distribution is utilized to analyze the E_b of AN, AG2N and AG2N+Mn ceramics, as shown in Fig. 1b. The calculation formulas are as follows:[19,28]

$$X_i = \ln(E_i) \quad (5)$$

$$Y_i = \ln\left(\ln\frac{1}{1-P_i}\right) \quad (6)$$

$$P_i = \frac{i}{n+1} \quad (7)$$

where X_i and Y_i are two variables, E_i is the E_b of the ith given sample and is arranged in ascending order. P_i is the probability of dielectric breakdown. All data fits conform to a good linear relationship and the Weibull modulus β of all compositions is larger than 19, demonstrating high reliability of the Weibull analysis. The relationship between E_b and grain size is shown in Fig.1c. E_b gradually increases from 200 kV cm^{-1} to 250 kV cm^{-1} with the additions of 2 mol% Gd and 0.3 wt% Mn. When 2 mol% Gd is added, the E_b increases from 200 to 230 kV cm^{-1}, and when 2 mol% Gd and 0.3 wt% Mn are added, the E_b is further increased to 250 kV cm^{-1}. This is attributed to the high density and reduced leakage current. It is clearly observed from SEM images that the doping of Gd effectively reduces the grain size. The reduction of grain size produces a large number of grain

DOI: 10.54227/mlab.20230014

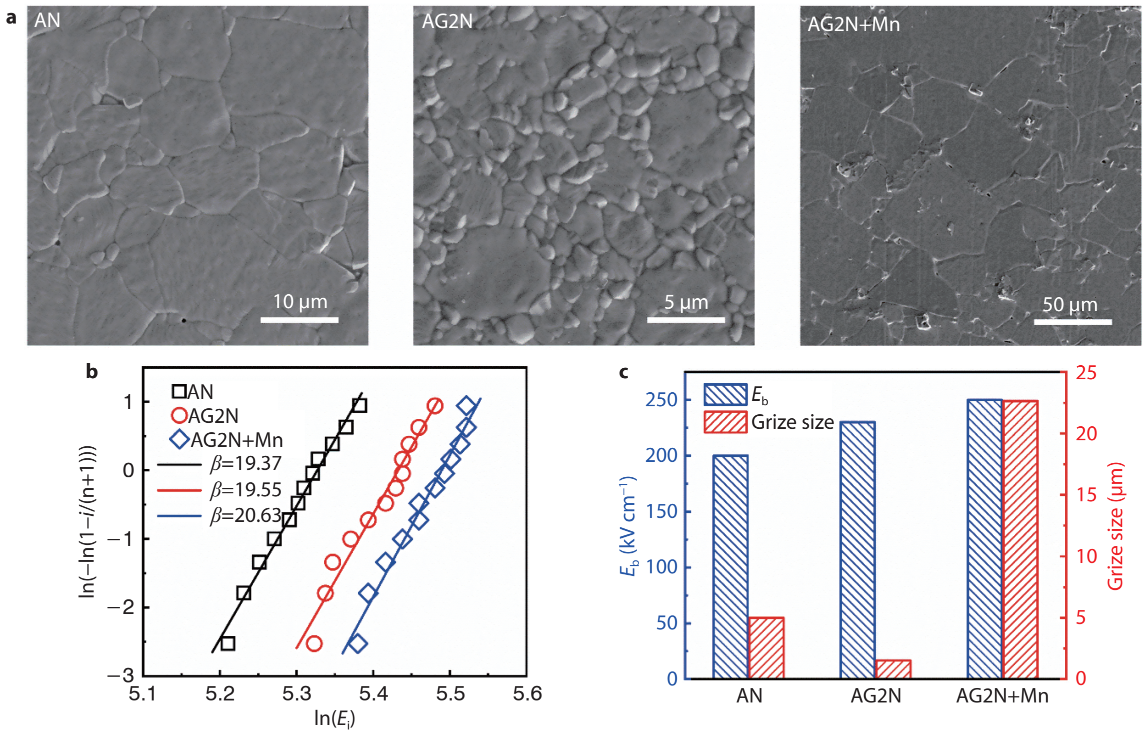

Fig. 1 **a** SEM, **b** Weibull plots of E_b, **c** grain size and E_b of AN, AG2N and AG2N+Mn ceramics.

boundaries. The grain boundaries would cause depletion of space charge layers, which can prevent the carriers from crossing the grain boundaries.[30] A large number of grain boundaries will increase the resistance and effectively improve E_b.[31] But the E_b increases in Mn-doped ceramic with enlarged grain size, which may be attributed to the reduced leakage current.

Fig. 2a(1) shows the XRD patterns of AN, AG2N and AG2N+Mn ceramics. All the samples exhibit a perovskite structure without any impurity phase, indicating Gd and Mn ions have diffused into AN lattices to form a solid solution. Fig. 2a(2) is enlarged (220)/(008) peaks. It can be inferred that the increased *d*-spacing of (008) planes can extend *c* axis of orthorhombic lattice, while the increased *d*-spacing of (220) planes can contribute to the increased *a* and *b* axes of orthorhombic lattice. According to the previous reports, the AFE displacement of AN is along the *b* axis of orthorhombic lattice.[32] With the incorporation of 2 mol% Gd, the (008) and (220) diffraction peaks become close. These results indicate that Gd doping should favor chemical pressure, which compresses the *a*/*b* axes and elongates the *c* axis of orthorhombic lattice, suggesting that Gd doping reduces the AFE displacement and enhances the AFE stability. In addition, the merge of (220)/(008) peaks in AG2N ceramic also implies the M_1-M_2 phase transition.[32] For Gd-doped AN ceramic, the defect reaction formula can be written as following:[33]

$$Gd_2O_3 + 3Nb_2O_5 \xrightarrow{AgNbO_3} 2Gd_{Ag}^{\cdot\cdot} + 4V'_{Ag} + 6Nb_{Nb}^{\times} + 18O_O^{\times}$$

The chemical formula indicates that the substitution of Gd for Ag at A-site would generate Ag vacancies in the AN lattice, which makes the reduction in the cell volume and inhibits the shift of Nb^{5+} and Ag^{+}, thereby enhancing the AFE stability.[26] After Mn-doping, the (220) peak moves to the high angle and the (008) peak moves to the low angle. This indicates that Mn ions have diffused into the AN lattice and resulted in the lattice shrinkage. The valence state of Mn ions is related to temperature. Mn ions reveal diverse valence at different temperatures: MnO_2 (<535 °C), Mn_2O_3 (<1080 °C), Mn_3O_4 (<1650 °C) and MnO (>1650 °C). When the sintering temperature is 1000 °C-1200 °C, Mn^{2+} and Mn^{3+} may coexist, but Mn^{4+} cannot be excluded. The Mn^{2+} (0.083 nm, CN = 6), Mn^{3+} (0.065 nm, CN =6) and Mn^{4+} (0.053 nm, CN = 6) could substitute either Ag^{+} (0.148 nm, CN = 12) at A-site or Nb^{5+} (0.064 nm, CN = 6) at B-site or both. The shrunken lattice indicates that the substitutions of Mn^{2+}/Mn^{3+}/Mn^{4+} for Ag^{+} are dominating. The complex substitution behavior of Mn ions has also been confirmed by a large number of reports.[27,34,35]

The phase structures of AN, AG2N and AG2N+Mn ceramics at room temperature are further investigated using Raman spectra as shown in Fig. 2b. According to different vibration modes, three characteristic peaks v_1, v_2 and v_5 are distinguished. v_1 represents the double degenerate symmetric tensile vibration of Nb-O, v_2 represents the nondegenerate symmetric tensile vibration of Nb-O, and v_5 represents the triple degenerate bending vibration of Nb-O. After Gd doping, v_1 and v_5 decrease in intensity and become wider in shape, indicating the disturbed long-range ordering of AN.[26] The attenuation of v_2 vibration peak indicates the improvement of symmetry and the suppression of ferroelectricity. Meanwhile, the disappeared peaks at 83, 205 and 632 cm^{-1} imply that the room-temperature phase structure changes from M_1 phase to M_2 phase.[6] The addition of Mn ions further reduces the radius of A-site ions and makes v_1 and v_5 lower in intensity and wider in shape.[35] These are consistent with the variation of XRD patterns.

Fig. 3a-c shows the dielectric constant (ε_r) and dielectric

DOI: 10.54227/mlab.20230014

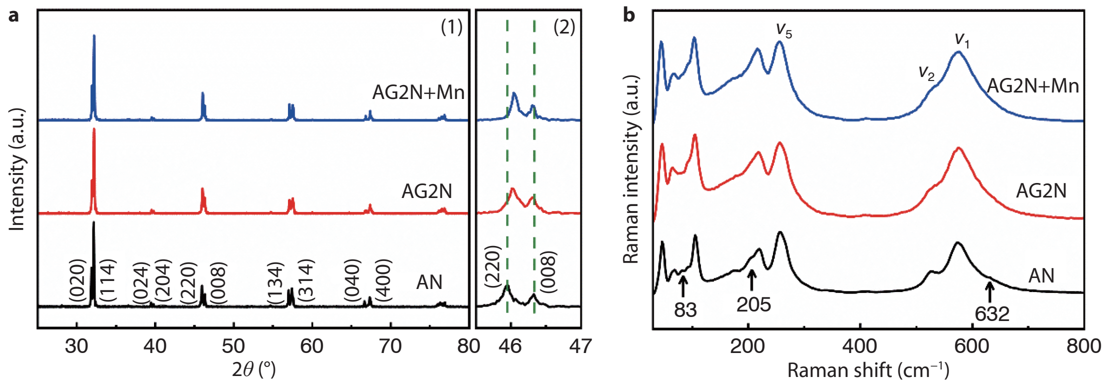

Fig. 2 **a(1)** XRD patterns, **a(2)** enlarged (220)/(008) peaks and **b** Raman spectra of AN, AG2N and AG2N+Mn ceramics.

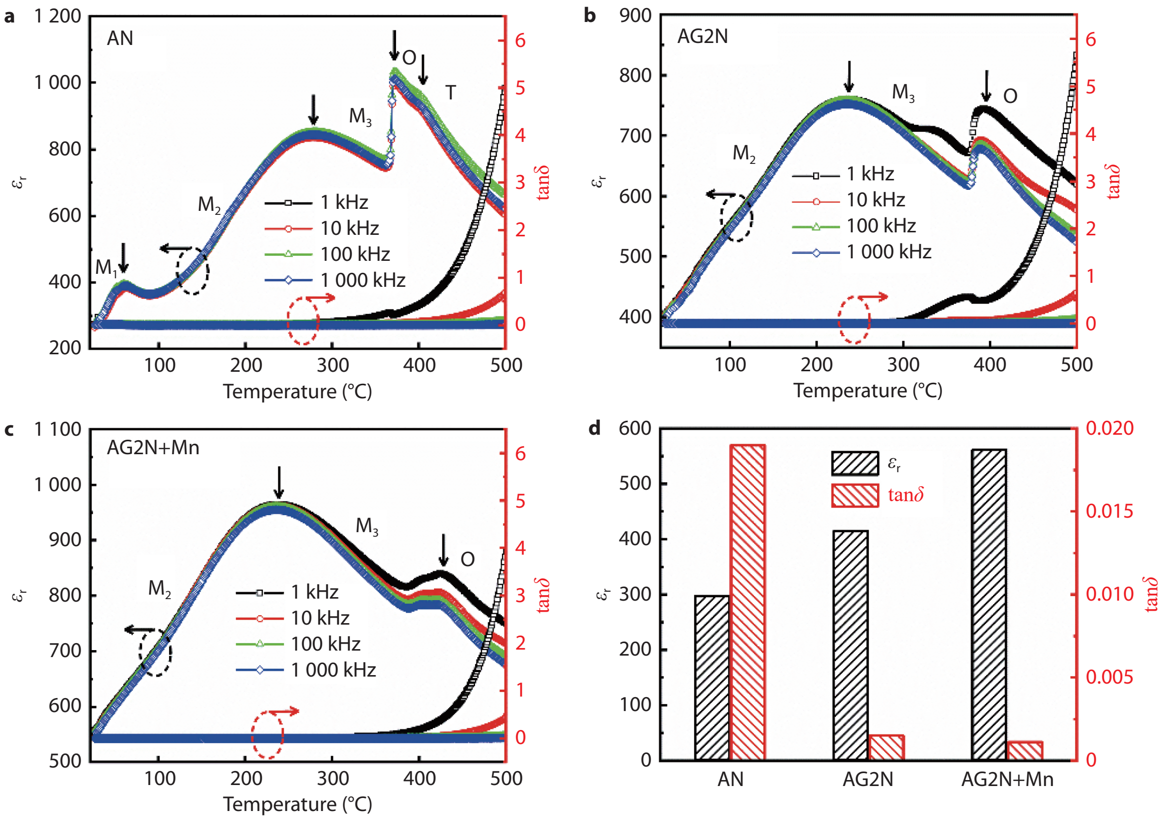

Fig. 3 Dielectric constant and dielectric loss of AN, AG2N, and AG2N+Mn ceramics **a-c** as a function of temperature and **d** at room temperature.

loss (tanδ) of AN, AG2N and AG2N+Mn ceramics as a function of temperature at 1-1000 kHz. There are four dielectric anomaly peaks corresponding to M_1-M_2-M_3-O-T phase transitions in AN ceramic.[9,36] Pure AN ceramic is M_1 phase at room temperature. The main phase transition temperature is shown in Table 1. T_{M1-M2} and T_{M2-M3} decrease after Gd doping, which makes AG2N ceramic in M_2 phase at room temperature, indicating that the FIE phase is weakened and the AFE phase is enhanced in AG2N ceramic. After the addition of Mn, T_{M2-M3} does not change significantly. It is obvious that the ε_r of M_2 phase is generally higher than that of M_1 phase as shown in Fig. 3a. The addition of Gd results in an increased ε_r up to 415 at room temperature as shown in Fig. 3d. This is because the T_{M1-M2} is lower to room temperature after Gd doping, which makes a higher ε_r in M_2 phase. The ε_r is further increased to 562 after Mn doping. The increased ε_r may be attributed to the increased silver vacancies caused by Mn doping, which tends to result in "soft" doping to enhance the polarization.[37] In addition, the tanδ sharply decreases after Gd and Mn doping. The decrease in tanδ is attributed to avoiding the phase transition at room temperature.[11]

The *P-E* loops of AN, AG2N and AG2N+Mn ceramics are tested at a frequency of 10 Hz. All the ceramics show typical double *P-E* loops as shown in Fig. 4a. More details are shown in Fig. 4b and c. The P_{max} and P_r are 61.1 and 8.9 μC cm^{-2} for pure AN ceramic, which decreases to 56.6 and 5 μC cm^{-2} after

Table 1. Phase transition temperatures of AN, AG2N and AG2N+Mn ceramics.

Samples	$T_{M1\text{-}M2}$ (°C)	$T_{M2\text{-}M3}$ (°C)	$T_{M3\text{-}O}$ (°C)	$T_{O\text{-}T}$ (°C)
AN	60	278	370	401
AG2N	/	235	392	437
AG2N+Mn	/	236	427	/

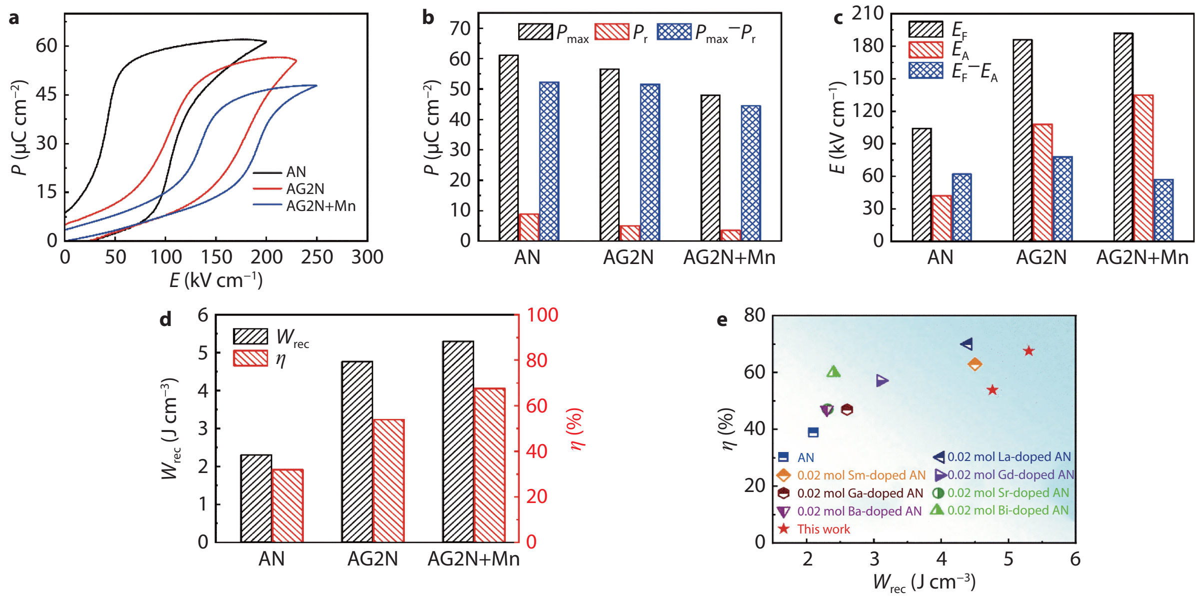

Fig. 4 **a** *P-E* loops, **b** P_{max}, P_r, and P_{max}-P_r, **c** E_F, E_A, and E_F-E_A, and **d** W_{rec}, η of AN, AG2N and AG2N+Mn ceramics at 10 Hz. **e** W_{rec} and η of reported AN-based ceramics.

2 mol% Gd adding. At the same time, P_{max}-P_r decreases from 52.2 to 51.6 μC cm^{-2}. After adding Mn, P_{max}, P_r and P_{max}-P_r are further reduced to 48.0, 3.5 and 44.5 μC cm^{-2}. The decrease in polarization indicates the enhancement of AFE stability. The enhanced AFE stability is also confirmed by the varied E_A and E_F. The E_A and E_F are 42 and 104 kV cm^{-1} for pure AN ceramic, which increase to 108 and 186 kV cm^{-1} after 2 mol% Gd doping. While the E_F-E_A slightly decreases from 62 to 78 kV cm^{-1}. Both the increased E_A and reduced E_F-E_A are good for the energy storage performance. After adding Mn, E_A and E_F are increased to 135 and 192 kV cm^{-1}, respectively. E_F-E_A decreases to 57 kV cm^{-1}, which is conducive to the improvement of η. The W_{rec} and η are calculated as shown in Fig. 4d. The W_{rec} and η reach 5.3 J cm^{-2} and 67.6% as a combined effect of Gd and Mn. They are 2.3 and 2.1 times of pure AN (W_{rec}=2.3 J cm^{-3}, η=31.9%), respectively. In addition, both the AG2N and AG2N+Mn ceramics show better W_{rec} than those reported AN-based ceramics with 2 mol% ion-doping in A-site as shown in Fig. 4e.[17,24–26,38–40]

The temperature stability is a key indicator in practical applications. Fig.5a shows the *P-E* loops of AG2N+Mn ceramics at 30-170 °C under 250 kV cm^{-1} and 10 Hz. With the increase in temperature, the *P-E* loops gradually become progressively slimmer. The AG2N+Mn ceramic shows better *P-E* loops at 30-130 °C. The *P-E* loops are deteriorated at 150-170 °C, which is due to the increase of leakage current. Fig. 5b shows the variations of P_r, P_{max}, and P_{max}-P_r with temperature. At 30-110 °C, both P_r and P_{max} gradually increase and P_{max}-P_r remains stable in AG2N+Mn ceramic. With the increase in temperature, the movement of domain walls becomes easier, making P_r and P_{max} increase. In addition, various defects are gradually activated at high temperatures, resulting in an increase in the leakage current of the ceramic, which also contributes to the increased P_r and P_{max}.[41] However, when the temperature exceeds 130 °C, P_{max} decreases, which may be caused by the phase transition. It is speculated that the M_2-M_3 phase transition may occur since M_3 phase has more stable antiferroelectricity than M_2 phase, which would lead to reduced P_{max}. E_F first decreases and then increases with temperature with a turning point at 130 °C as shown in Fig. 5c. The decreased E_F at 30-130 °C is due to the fact that increasing the temperature can reduce the potential barrier of AFE-FE phase transition, making the phase transition easier. The increased E_F at 130-170 °C may be caused by M_2-M_3 phase transition.[11] E_A shows an upward trend with the increase in temperature. On the one hand, high temperature is conducive to short-range interaction, which makes AFE phase more stable.[22] On the other hand, the M_2-M_3 phase transition will also enhance the AFE stability. E_F-E_A keeps a decreasing trend, which is conducive to the improvement of η. It is speculated that the M_2-M_3 phase transition occurs at 130 °C when the applied electric field is 250 kV cm^{-1}. W_{rec} remains 5.3-5.1 J cm^{-3} at 30-110 °C and reduces to 4.6 J cm^{-3} at 130-170 °C due to the reduced P_{max}-P_r. η is reduced from 67.6% to 62.3% in the temperature range of 30-170 °C with a variation of less than 8.2%.

Fig. 6a plots the frequency dependence of the *P-E* loops under 240 kV cm^{-1}. At 5-200 Hz, the *P-E* loops gradually become thinner. More details are shown in Fig. 6b and c. With the increase of frequency, P_{max} decreases from 42.6 to 37.4 μC cm^{-2}, and P_r decreases from 2.9 to 1.2 μC cm^{-2}, resulting in

DOI: 10.54227/mlab.20230014

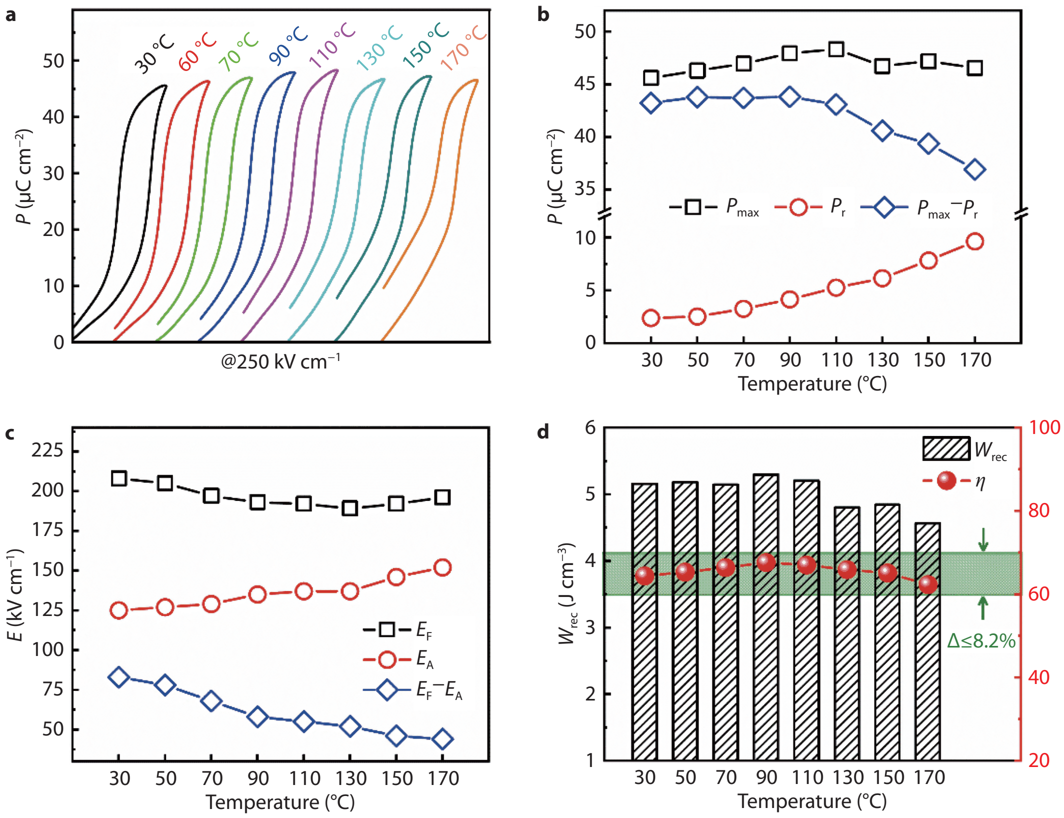

Fig. 5 **a** *P-E* loops, **b** P_r, P_{max}, and P_{max}-P_r, **c** E_F, E_A, and E_F-E_A, and **d** W_{rec} and η of AG2N+Mn ceramics during 30-170 °C under 250 kV cm^{-1}.

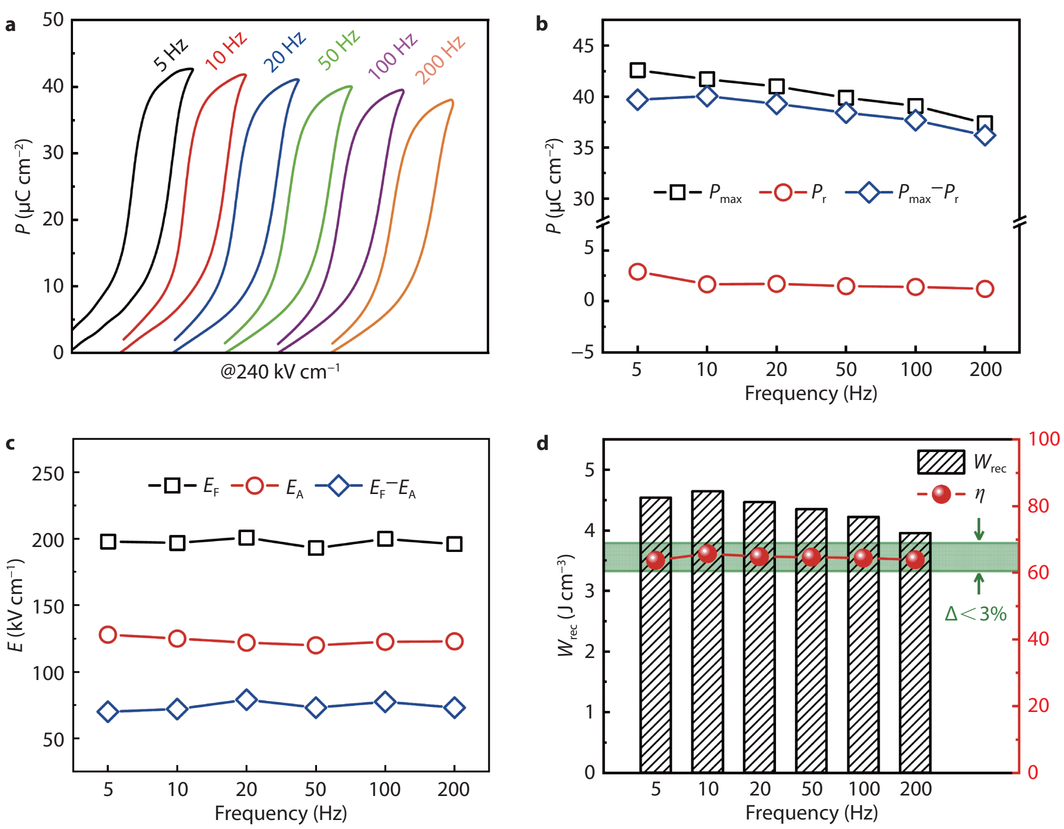

Fig. 6 **a** *P-E* loops, **b** P_{max}, P_r, and P_{max}-P_r, **c** E_F, E_A, and E_F-E_A, and **d** W_{rec} and η of AG2N+Mn ceramics during 50-200 Hz under 240 kV cm^{-1}.

DOI: 10.54227/mlab.20230014

the decrease of P_{max}-P_r from 39.7 to 36.2 μC cm^{-2}. The reason for the decrease of P_{max} is that the action time of the electric field at a higher frequency is shorter, some FE domain inversion is not completed, and AFE stability is enhanced.[42] E_F and E_A fluctuate in a small range and remain stable on the whole. As shown in Fig. 6d, the W_{rec} is reduced from 4.7 J cm^{-3} to 4.0 J cm^{-3}, and the η is reduced from 63.9% to 65.7% with a variation of less than 3%.

Conclusions

In summary, high-quality Gd and Mn doped AN ceramics are prepared using the tape casting method. The introduction of Gd can effectively reduce the grain size and increase E_b. Gd doping makes M_2 phase more stable at room temperature and improves AFE stability. Enhanced AFE stability yields a high W_{rec} of 4.76 J cm^{-3} with η of 53.9% in AG2N ceramic. MnO_2 is introduced to improve E_b and AFE stability, and reduce dielectric loss, which further optimizes the energy storage performance. A large W_{rec} of 5.3 J cm^{-3} with η of 67.6% is achieved in Mn-doped AG2N ceramic. In addition, the W_{rec} shows good temperature stability and frequency stability. These results show that the components and processes proposed in this work provide a feasible method for improving the energy storage performance.

■ ACKNOWLEDGEMENTS

This work was supported by the Natural Science Foundation of Hebei Province, China (No. E2021201044), the National Natural Science Foundation of China (No.51802068 and No.52073144).

■ CONFLICT OF INTEREST

The authors declare no conflict of interest.

■ REFERENCES

1. J. W. Choi, D. Aurbach, *Nat. Rev. Mater.*, 2016, 1, 16013
2. W. J. Sun, J. Mao, S. Wang, L. Zhang, Y. H. Cheng, *Front. Chem. Sci. Eng.*, 2021, 15, 18
3. J. J. Ma, J. Zhang, J. Guo, X. J. Li, S. Guo, Y. Huan, J. Wang, S. T. Zhang, Y. J. Wang, *Chem. Mater.*, 2022, 34, 7313
4. H. Palneedi, M. Peddigari, G. T. Hwang, D. Y. Jeong, J. Ryu, *Adv. Funct. Mater.*, 2018, 28, 1803665
5. A. R. Jayakrishnan, J. P. B. Silva, K. Kamakshi, D. Dastan, V. Annapureddy, M. Pereira, K. C. Sekhar, *Prog. Mater. Sci.*, 2023, 132, 101046
6. M. Y. Zhao, J. Wang, H. Yuan, Z. H. Zheng, L. Zhao, *J. Materiomics*, 2023, 9, 19
7. Z. M. Dang, J. K. Yuan, S. H. Yao, R. J. Liao, *Adv. Mater.*, 2013, 25, 6334
8. H. S. wang, Y. C. Liu, T. Q. Yang, S. J. Zhang, *Adv. Funct. Mater.*, 2019, 29, 1807321
9. B. Xu, J. Íñiguez, L. Bellaiche, *Nat. Commun.*, 2017, 8, 15682
10. H. Y. He, X. Lu, E. Hanc, C. Chen, H. Zhang, L. Lu, *J. Mater. Chem. C*, 2020, 8, 1494
11. Y. Tian, L. Jin, Q. Y. Hu, K. Yu, Y. Y. Zhang, G. Viola, I. Abrahams, Z. Xu, X. Y. Wei, H. X. Yan, *J. Mater. Chem. A*, 2019, 7, 834
12. Y. B. Fan, W. J. Wang, J. Y. Zhao, *Ceram. Int.*, 2020, 46, 12269
13. X. He, C. Chen, C. B. Li, H. R. Zeng, Z. G. Yi, *Adv. Funct. Mater.*, 2019, 29, 1900918
14. L. Chen, M. Y. Zhao, J. Wang, S. W. Zhang, F. H. Sun, L. Zhao, *J. Materiomics*, 2022, 8, 863
15. Y. Tian, P. P. song, G. Viola, J. D. Shi, J. Li, L. Jin, Q. Y. Hu, Y. H. Xu, W. Y. Ge, Z. N. Yan, D. Zhang, N. V. Tarakina, I. Abrahams, X. Y. Wei, H. X. Yan, *J. Mater. Chem. A*, 2022, 10, 14747
16. D. S. Fu, M. Endo, H. Taniguchi, T. Taniyama, M. Itoh, *Appl. Phys. Lett.*, 2007, 90, 252907
17. Y. Tian, L. Jin, H. F. Zhang, Z. Xu, X. Y. Wei, E. D. Politova, S. Y. Stefanovich, N. V. Tarakina, S. Abrahams, H. X. Yan, *J. Mater. Chem. A*, 2016, 4, 17279
18. L. Zhao, Q. Liu, J. Gao, S. J. Zhang, J. F. Li, *Adv. Mater.*, 2017, 29, 1701824
19. L. Zhao, J. Gao, Q. Liu, S. J. Zhang, J. F. Li, *ACS Appl. Mater. Interfaces*, 2018, 10, 819
20. D. Yang, J. Gao, L. Shu, Y. Liu, J. Yu, Y. Zhang, X. Wang, B. Zhang, J. F. Li, *J. Mater. Chem. A*, 2020, 8, 23724
21. N. N. Luo, K. Han, F. Zhuo, C. Xu, G. Zhang, L. Liu, X. Chen, C. Hu, H. Zhou, Y. Wei, *J. Mater. Chem. A*, 2019, 7, 15450
22. M. Y. Zhao, J. Wang, H. Yuan, Z. H. Zheng L. Zhao, *ACS Appl. Mater. Interfaces*, 2022, 14, 48926
23. N. N. Luo, K. Han, L. J. Liu, B. L. Peng, X. P. Wang, C. Z. Hu, H. F. Zhou, Q. Feng, X. Y. Chen, Y. Z. Wei, *J. Am. Ceram. Soc.*, 2019, 102, 4640
24. J. Gao, Y. C. Zhang, L. Zhao, K. Y. Lee, Q. Liu, A. Studer, M. Hinterstein, S. J. Zhang, J. F. Li, *J. Mater. Chem. A*, 2019, 7, 2225
25. J. Gao, Q. Liu, J. F. Dong, X. P. Wang, S. J. Zhang, J. F. Li, *ACS. Appl. Mater. Interfaces*, 2020, 12, 6097
26. S. Li, H. C. Nie, G. S. Wang, C. H. Xu, N. T. Liu, M. X. Zhou, F. Cao, X. L. Dong, *J. Mater. Chem. C*, 2019, 7, 1551
27. L. Zhao, Q. Liu, S. Zhang, J. F. Li, *J. Mater. Chem. C*, 2016, 4, 8380
28. M. Y. Zhao, J. Wang , L. Chen, H. Yuan, M. H. Zhang, S. W. Zhang, L. Zhao, *Rare Metals*, 2023, 42, 495
29. P. Peng, H. C. Nie, Z. Liu, W. J. Ren, F. Cao, G. S. Wang, X. L. Dong, *J. Am. Ceram. Soc.*, 2017, 100, 1030
30. R. Waser, *Ferroelectrics*, 1992, 133, 109
31. Z. H. Yao, Z. Song, H. Hao, Z. Y. Yu, M. H. Cao, S. J. Zhang, M. T. Lanagan, H. X. Liu, *Adv. Mater.*, 2017, 29, 1601727
32. Y. Tian, P. P. Song, R. Gu, Y. H. Xu, L. Jin, T. Wang, X. Y. Wei, W. Y. Ge, *Ceram. Int.*, 2022, 48, 32703
33. G. Du, R. Liang, L. Wang, K. Li, W. Zhang, G. Wang, X. Dong, *Appl. Phys. Lett.*, 2013, 102, 162907
34. X. Fan, D. Lin, Q. Zheng, H. Sun, Y. Wan, X. Wu and L. Wu, *Phys. Status Solidi A.*, 2012, 209, 2610
35. C. H. Xu, Z. Q. Fu, Z. Liu, L. Wang, S. G. Yan, X. F. Chen, F. Cao, X. L. Dong, G. S. Wang, *ACS Sustainable Chem. Eng.*, 2018, 6, 16151
36. I. Levin, V. Krayzman, J. C. Woicik, J. Karapetrova, T. Proffen, M. G. Tucker, I. M. Reaney, *Phys. Rev. B*, 2009, 79, 104113
37. L. Jin, F. Li, S. J. Zhang, *J. Am. Ceram. Soc.*, 2014, 97, 1
38. N. N. Luo, K. Han, F. P. Zhuo, L. J. Liu, X. Y. Chen, B. Peng, X. Wang, Q. Feng, Y. Z. Wei, *J. Mater. Chem. C*, 2019, 7, 4999
39. K. Han, N. N. Luo, S. F. Mao, F. Zhuo, X. Chen, L. Liu, C. Hu, H. Zhou, X. Wang, Y. Z. Wei, *J. Materiomics*, 2019, 5, 597
40. Y. Tian L. Jin, H. Zhang, Z. Xu, X. Wei, G. Viola, I. Abrahams, H. X. Yan, *J. Mater. Chem. A*, 2017, 5, 17525
41. J. P. Shi, X. L. Chen, X. Li, J. Sun, C. C. Sun, F. H. Pang, H. F. Zhou, *J. Mater. Chem. C*, 2020, 8, 3784
42. J. Jiang, X. J. Meng, L. Ling, S. Guo, M. Huang, J. Zhang, J. Wang, X. H. Hao, H. G. Zhu, S. T. Zhang, *Energy Storage Mater.*, 2021, 43, 383

©2023 The Authors. *Materials Lab* is published by Lab Academic Press. This is an open access article under the terms of the Creative Commons Attribution License, which permits use, distribution and reproduction in any medium, provided the original work is properly cited.